

A flux-matched gyrokinetic analysis of DIII-D L-mode turbulence

T. Görler, A. E. White, D. Told, F. Jenko, C. Holland, and T. L. Rhodes

Citation: *Physics of Plasmas* (1994-present) **21**, 122307 (2014); doi: 10.1063/1.4904301

View online: <http://dx.doi.org/10.1063/1.4904301>

View Table of Contents: <http://scitation.aip.org/content/aip/journal/pop/21/12?ver=pdfcov>

Published by the [AIP Publishing](#)

Articles you may be interested in

[Multi-field characteristics and eigenmode spatial structure of geodesic acoustic modes in DIII-D L-mode plasmas](#)

Phys. Plasmas **20**, 092501 (2013); 10.1063/1.4819501

[Simulations of drift resistive ballooning L-mode turbulence in the edge plasma of the DIII-D tokamaka\)](#)

Phys. Plasmas **20**, 055906 (2013); 10.1063/1.4804638

[Multi-field/multi-scale turbulence response to electron cyclotron heating of DIII-D ohmic plasmas](#)


Phys. Plasmas **18**, 082504 (2011); 10.1063/1.3610552


[Response of multiscale turbulence to electron cyclotron heating in the DIII-D tokamaka\)](#)

Phys. Plasmas **14**, 056117 (2007); 10.1063/1.2714019


[Analysis of metallic impurity density profiles in low collisionality Joint European Torus H-mode and L-mode plasmas](#)

Phys. Plasmas **13**, 042501 (2006); 10.1063/1.2187424

A collection of five pieces of Pfeiffer Vacuum equipment: a red turbopump, a silver turbopump, a silver backing pump, a red turbopump with a long shaft, and a silver chamber component.

 Vacuum Solutions from a Single Source

- Turbopumps
- Backing pumps
- Leak detectors
- Measurement and analysis equipment
- Chambers and components

PFEIFFER  **VACUUM**

A flux-matched gyrokinetic analysis of DIII-D L-mode turbulence

T. Görler,^{1,a)} A. E. White,² D. Told,¹ F. Jenko,^{1,3} C. Holland,⁴ and T. L. Rhodes³

¹Max Planck Institute for Plasma Physics, Boltzmannstr. 2, 85748 Garching, Germany

²Massachusetts Institute of Technology, Cambridge, Massachusetts 02139, USA

³Department of Physics and Astronomy, University of California, Los Angeles, California 90095, USA

⁴Center for Energy Research, University of California, San Diego, 9500 Gilman Drive, La Jolla, California 92093, USA

(Received 30 September 2014; accepted 12 November 2014; published online 17 December 2014)

Previous nonlinear gyrokinetic simulations of specific DIII-D L-mode cases have been found to significantly underpredict the ion heat transport and associated density and temperature fluctuation levels by up to almost one order of magnitude in the outer-core domain, i.e., roughly in the last third of the minor radius. Since then, this so-called *shortfall* issue has been subject to various speculations on possible reasons and furthermore motivation for a number of dedicated comparisons for L-mode plasmas in comparable machines. However, only a rather limited number of simulations and gyrokinetic codes has been applied to the original scenario, thus calling for further dedicated investigations in order to broaden the scientific basis. The present work contributes along these lines by employing another well-established gyrokinetic code in a numerically and physically comprehensive manner. Contrary to the previous studies, only a mild underprediction is observed at the outer radial positions which can furthermore be overcome by varying the ion temperature gradient within the error bars associated with the experimental measurement. The significance and reliability of these simulations are demonstrated by benchmarks, numerical convergence tests, and furthermore by extensive validation studies. The latter involve cross-phase and cross-power spectra analyses of various fluctuating quantities and confirm a high degree of realism. The code discrepancies come as a surprise since the involved software packages had been benchmarked repeatedly and very successfully in the past. Further collaborative effort in identifying the underlying difference is hence required. [<http://dx.doi.org/10.1063/1.4904301>]

I. INTRODUCTION

The energy and particle confinement in tokamaks are mainly limited by small-scale turbulent transport caused by steep temperature and density gradients. Due to the high temperatures and thus low-collisionality on the one hand and the existence of strong background magnetic fields, the gyrokinetic theory¹ is established as the most appropriate theoretical description, see, e.g., Refs. 2 and 3 and references therein. However, solutions of the underlying nonlinear system of equations in 5D phase space can generally only be obtained numerically, and hence a number of corresponding implementations with different numerical approaches and different degrees of physical comprehensiveness exists.² However, the ultimate and common goal is to finally develop a predictive capability for present and future fusion experiments and to support the optimization and actual design of the devices and the diagnostics. As early gyrokinetic simulations could only be run with reduced physics models—e.g., by using simplified magnetic equilibria, adiabatic electrons, etc.—they were mainly restricted to qualitative statements. Though some results were already quite impressive, the last decade has seen major improvements and extensions such that by now quantitative comparisons with experiments can be carried out. Hence, the great opportunity to not only verify but also validate the numerical tools and the gyrokinetic theory itself can be utilized.

Pioneering work along these lines can, for instance, be found in Refs. 4–7 where particularly H- and QH-mode but also L-mode plasmas could successfully be assessed with the gyrokinetic code GYRO at various radial positions.⁸ However, similar validation attempts in the outer-core domain (i.e., in about the last third of the minor radius) of a small number of DIII-D tokamak⁹ L-mode discharges failed to reproduce the experimental heat flux levels.^{10,11} One of the first and most detailed publications in this context is Ref. 10 where a significant ion heat transport underprediction or *shortfall* is reported. Here, the same code as for the aforementioned successful validation studies for different physical scenarios has been employed. Consequently raised concerns that this transport shortfall might be rather universal to L-mode modeling and thus point to missing or incorrect physics within the gyrokinetic codes or the theory itself could meanwhile be repealed partially. In Ref. 11, for instance, a slight underprediction can only be seen at lower electron-to-ion temperature $T_e/T_i \sim 1$ while at high T_e/T_i even a slight overprediction can be observed. Similar studies for L-modes in other machines, e.g., for Alcator C-MOD,¹² NSTX,¹³ and in a joint project of two different gyrokinetic codes for ASDEX Upgrade,¹⁴ could not reproduce the ion heat transport underprediction; while such discrepancies in the electron heat flux have been observed in some cases. However, as the latter may be attributed to the typically neglected electron gyroradius scales, only the ion heat transport underprediction is labeled as *shortfall* in the following.

^{a)}Electronic mail: tobias.goerler@ipp.mpg.de

Albeit the recent restrictions for a shortfall scenario, the original findings are puzzling and give rise to concerns whether neglected non-local effects like turbulence spreading,¹¹ the suppression of higher-order nonlinear effects retained in full-*f* codes, or the application of gyrokinetics per se should be reconsidered for the DIII-D case and similar discharges.¹⁵ As the published data is currently mostly based on the results of a single gyrokinetic code with only a few data points contributed from another one,¹¹ it is of prime importance to involve other groups and broaden or constrain the scientific basis for the aforementioned concerns.

This contribution aims at bridging this gap by applying a numerically different but physically similar comprehensive code to the same L-mode scenario as described above. In this context, advantage is taken from the fact that both implementations have already successfully passed a number of intercode comparisons in the past—see, e.g., Refs. 16–18 for the popular Cyclone benchmark, small-scale (electron temperature gradient, ETG) mode, and electromagnetic turbulence comparisons. However, none of these studies has either reached this level of comprehensiveness as required here or addressed independent and comprehensive validation attempts.

The rest of the paper is organized as follows. In Sec. II, the physical scenario is discussed in detail and the numerical tool and relevant observables are reviewed. A characterization of the main microinstabilities in the considered L-mode discharge is found in Sec. III before the nonlinear gyrokinetic simulation results regarding the turbulent transport are presented in Sec. IV. These results are further substantiated by validation against experimental measurements in Sec. V. Conclusions are presented in Sec. VI.

II. PHYSICAL SCENARIO AND NUMERICAL TOOLS

A. Experimental setup

In the following, one of the first and hence quite prominent gyrokinetic investigations reporting a shortfall¹⁰ will be reassessed and discussed in detail employing an alternative and independent code package. Before introducing the latter, the physical scenario shall be reviewed briefly.

Subject of this study is DIII-D discharge #128913 which has first been presented in Refs. 19 and 20. This L-mode plasma is characterized by an upper single-null shape, i.e., by a deliberately chosen unfavorable ∇B drift configuration preventing transition into H-mode. Its line-averaged electron density is $n_e = 2.3 \times 10^{13} \text{ cm}^{-3}$, while on-axis parameters are $n_e = 3.4 \times 10^{13} \text{ cm}^{-3}$, $T_e = 2.6 \text{ keV}$, and $T_i = 1.9 \text{ keV}$. The toroidal field on axis is $B_0 = 2.1 \text{ T}$ and the plasma current $I_p = 1 \text{ MA}$. A single coinjected neutral beam has been applied to deposit a heating power of 2.5 MW. The time slice considered for the magnetic equilibrium and the profiles is $t = 1.5 \text{ s}$. While preliminary simulation results and a first remark regarding a transport underprediction are presented in the above references, a detailed description regarding the numerical setup and the results can be found in Ref. 10. Two radial positions, namely, $\rho = 0.5$ and $\rho = 0.75$, are considered where ρ denotes the square root of the toroidal flux being normalized to its separatrix value. While good agreement between

the measured and simulated ion heat transport levels is found at the inner position, an underprediction by a factor of 7 is reported at $\rho = 0.75$. It shall also be mentioned that the half-radius position has been considered in detail in an intercode benchmark presented in Ref. 21 in the electrostatic and rotation-free limit. With respect to the ion heat flux, the code results agree reasonably well within 20% (30%) without (with) collisions. Naturally, these results form a solid basis to be reproduced in the present study.

B. Numerical tools and observables

The tool at hand for this purpose is the Eulerian nonlinear gyrokinetic code GENE^{22,23} which solves the gyrokinetic Vlasov equation coupled self-consistently to Maxwell's equations either in a flux-tube or in a (wide) radial annulus simulation domain. The former option—which benefits from spectral methods in both directions perpendicular to the magnetic field thus being numerically very robust and efficient—represents an appropriate choice if the gyroradii are small compared to the machine size and to the gradient length scale variations.^{24,25} In the given context, these requirements appear to be fulfilled for all radial positions under consideration. Unless stated otherwise, all simulations are considering fully gyrokinetically treated deuterium ions and electrons, electromagnetic effects by solving for the parallel component of Ampère's law, a finite Debye length, full inter- and intra-species collisions modeled by a linearized Landau-Boltzmann collision operator,²⁶ geometry information directly taken from the geqdsk efit file by field line tracing,²⁷ parallel flow shear, and—after a first sufficiently long initial saturation phase— $E \times B$ shear flow effects via time-dependent radial wave numbers as described in Ref. 28. The physical input parameters are derived from the DIII-D database files using 3rd order Lagrange interpolation. Numerical dissipation is only activated along the parallel direction where a fourth order centered finite difference scheme is employed for the derivatives, not in the perpendicular direction as is sometimes chosen in order to avoid spectral pile-ups due to unresolved scales. The latter effect is found to be reasonably small a posteriori.

Results of nonlinear simulations are typically time-averaged over a range of at least $200 \alpha / c_s$ in the quasi-stationary state. Here, the reference length $\alpha = (\Psi_{\text{tor,sep}} / \pi B_{\text{ref}})^{1/2}$ denotes the unnormalized ρ value corresponding to the toroidal flux $\Psi_{\text{tor,sep}}$ at the separatrix and the magnetic field on axis B_{ref} . Typically, α is comparable but not identical to the tokamak minor radius a . The ion sound speed is given by $c_s = \sqrt{T_e / m_i}$ and can be used to define the reference gyroradius as $\rho_s = c_s / \Omega_i$ with ion gyrofrequency $\Omega_i = q_i B_{\text{ref}} / (m_i c)$. Here, m_i denotes the ion mass, q_i its charge, and c the speed of light.

Statistical error bars for nonlinear, fluctuating quantities are defined similarly to Ref. 6 where the standard deviation of the mean values of consecutive temporal subdomains of the saturated state is proposed as a measure for the statistical uncertainty. The scheme is slightly extended as the subinterval time ranges are given by 5 correlation times (if more than ten intervals fit into the total time range; else two

correlation times). This way, averaging over the fast turbulence time scales should be established even for extreme cases while a time range fixed in simulation time units might be insufficient.

While a multitude of observables—e.g., density and parallel/perpendicular temperature fluctuations—can be tracked with GENE, the radial particle and heat transfer rates are the quantities of main interest in this context. Hence, their definition shall briefly be reviewed. Both observables are basically moments of the perturbed part of the particle center distribution function $f_1^{(pc)}$ which can be derived from the gyrocenter distribution function $f_1^{(gc)}$ via $f_{1\sigma}^{(pc)} = f_{1\sigma}^{(gc)} + [q_\sigma(\bar{\phi}_1^{(gc)} - \phi_1^{(pc)}) + \mu\bar{B}_{1\parallel}^{(gc)}]f_{0\sigma}/T_{0\sigma}$ with magnetic moment μ , background temperature $T_{0\sigma}$ and Maxwellian distribution function $f_{0\sigma}$ of the σ th species. The overbar denotes gyroaverages, the index 1 (0) indicates perturbed (equilibrium) quantities. With these definitions the particle and heat transfer rates read

$$\Gamma_\sigma = \left\langle \int d^3v f_{1\sigma}^{(pc)} \mathbf{v}_D \cdot \nabla x \right\rangle \cdot V', \quad (1)$$

$$P_\sigma = \left\langle \int d^3v \frac{1}{2} m_\sigma v^2 f_{1\sigma}^{(pc)} \mathbf{v}_D \cdot \nabla x \right\rangle \cdot V', \quad (2)$$

where the drift velocity \mathbf{v}_D is approximated by the general-ized $\mathbf{E} \times \mathbf{B}$ drift velocity, as in Ref. 10

$$\mathbf{v}_D \approx \frac{c}{B_0^2} \mathbf{B}_0 \times \nabla[\phi_1 - \mathbf{v} \cdot \mathbf{A}_1/c], \quad (3)$$

with vector field \mathbf{A}_1 . Here, $\langle \dots \rangle$ denotes flux surface averaging, x is the chosen radial coordinate (mostly, ρ), and $V' = \partial V/\partial x$ the radial derivative of the volume V enclosed by the (local) flux surface under consideration.

III. CHARACTERIZATION OF MICROINSTABILITIES

Though validations of gyrokinetic simulations vs. experiments are mainly based on turbulent transport fluxes, fluctuation levels or spectra which represent nonlinear features, linear investigations nevertheless provide a solid foundation and numerically inexpensive ground for such studies. First, they allow an easy characterization of the underlying micro-instabilities and the relevant scales. Second, they provide information on the required resolution in most of the parameter space. Third, sensitivities with respect to various input parameters can be assessed with much less effort and thus typically in much more detail than in nonlinear simulations.

A. Baseline parameter set

An overview regarding the most unstable growth rates and associated real frequencies determined by individual local simulations at a wide range of radial positions and toroidal mode numbers can be found in Fig. 1. Here and in the following linear investigations, $E \times B$ shear flow effects have been neglected due to the significantly more sophisticated analysis required in such cases. The resolution is at least $(n_k, n_z, n_{v\parallel}, n_\mu) = (9, 24, 48, 16)$ in terms of numerical radial

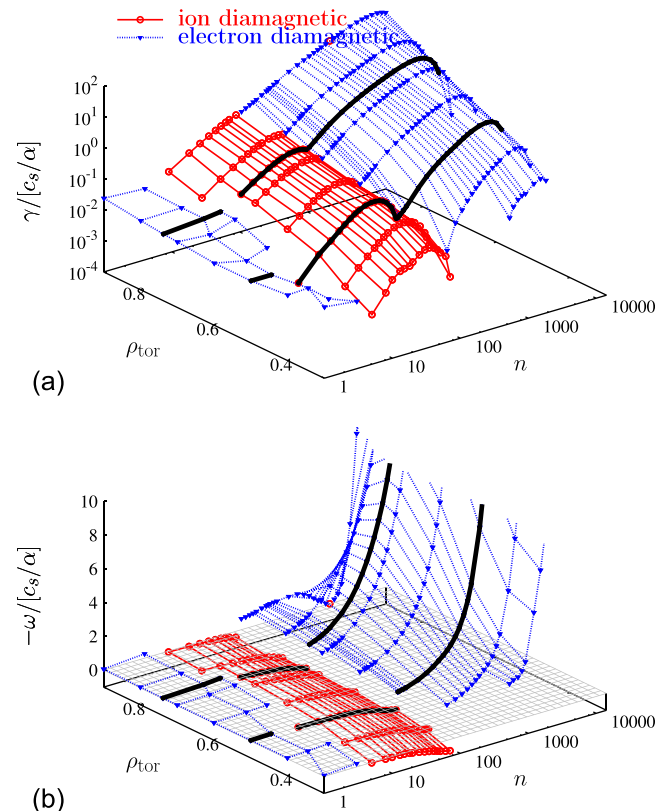


FIG. 1. Linear growth rate (a) and—for readability—negative frequency (b) vs. toroidal mode number n and radial coordinate ρ_{tor} for discharge 12 8913 at $k_r=0$. Here, the deuterium/electron mass ratio is used and collisional effects as well as a finite Debye wave length are taken into account, while $E \times B$ shear flow effects are neglected. Two radial positions which will be considered in more detail are marked by black lines and the zero frequency plane is depicted by gray lines.

wave numbers, parallel grid points, and (parallel velocity and magnetic moment) velocity space grid points, and convergence has been checked with scans at even higher resolution. The velocity space extends up to $(l_{v\parallel}, l_\mu) = (3v_{th,\sigma}, 9T_{0\sigma}/B_{\text{ref}})$, where $v_{th,\sigma} = \sqrt{2T_{0\sigma}/m_\sigma}$ denotes the thermal velocity of the σ th species with equilibrium temperature $T_{0\sigma}$ and mass m_σ . In these linear simulations, each k_x mode is coupled to $k_x=0$ via the parallel boundary condition such that the dominant mode has a physical wave number $k_r=0$. In Fig. 1, ion temperature gradient (ITG) driven modes—in GENE identified by a positive sign of the drift frequency indicating an ion diamagnetic drift and their sensitivity with respect to the logarithmic temperature gradient $\alpha/L_{Ti} = -\alpha \partial_x \ln T_i$ —can clearly be seen in the toroidal mode numbers range $n \sim 10$ –100 which corresponds to the ion-gyroradius scale. At smaller and larger scales, the dominant modes drift in the opposite direction, i.e., in the electron diamagnetic drift direction. Based on a parity-analysis of the mode structure, the large scale ($n \sim 1$ –5) instabilities can be identified as microtearing modes (MTM). As they appear to be only weakly driven, their transport contribution to the electron heat transport is most likely minor—the ion heat channel is typically only marginally affected by MTMs anyway. At larger wave numbers, smaller scales, respectively, trapped electron modes (TEMs) and ETG driven modes—partially transitioning smoothly into each other—prevail. Again their contribution to the ion heat transport is typically small.

However, it has been shown that MTMs^{29–31} and even the ETG driven electron-gyroradius-scale turbulence^{22,32,33} might cause substantial electron heat fluxes which has to be kept in mind if simulation results neglecting these scales and modes are compared with the experiment.

A rough rule-of-thumb which heuristically emerged from Refs. 33 and 34 and was successfully applied in Refs. 12 and 35 is to compare the growth rate peaks at ion- and electron-gyroradius-scales. Substantial ETG contributions are expected if the ratio is larger than the square root of the ion-to-electron mass ratio, $\sqrt{m_i/m_e}$. In the linear spectra at hand, the ratio appears to be close to this value at the outer radial position. Hence, ETG activity is expected but is most likely adding only modest electron heat transport fractions. However, the relevance of ETG might increase with $E \times B$ flow shear suppressing mainly large scale turbulence and slightly decrease if impurities are taken into account.

A final conclusion regarding the MTM and ETG mode contributions would require full-physics multiscale simulations reaching from supra-ion-down sub-electron-gyroradius-scales, a task which is virtually impossible with present-day computing resources. However, as the effects on the ion heat channel are most likely weak, nonlinear simulations targeting at just accurately modeling this channel can be restricted to a significantly reduced wave number range which roughly spans $n \sim 10$ –100.

For comparison, the two radial positions ($\rho = 0.5$ and $\rho \approx 0.75$) considered in previous publications are marked with black lines and the main physics input parameters being extracted from the ONETWO profiles are additionally listed in Table I for reference.

Particularly, the outer one where a shortfall has been reported in Ref. 10 shall be considered in more detail. Its

TABLE I. List of local parameters at the radial positions $\rho = 0.5$ and $\rho = 0.7386$ which will be of particular interest in Secs. IV–VI. All of them have directly been derived from the ONETWO profiles by GENE's internal profile interface.

$\rho = \rho_{\text{tor}}/\alpha$	0.5	0.7386
r/a	0.558	0.803
q	1.810	2.766
$\hat{s} = \rho \partial_\rho \ln q$	0.560	1.791
$\alpha/L_{T_i} = -\partial_\rho \ln T_i$	1.954	2.384
$\alpha/L_{T_e} = -\partial_\rho \ln T_e$	2.810	4.613
$\alpha/L_n = -\partial_\rho \ln n$	1.163	1.034
T_i/T_e	0.828	1.175
Z_{eff}	1.323	1.334
$\beta_{\text{ref}} = 8\pi n_e T_e / B_{\text{ref}}^2$	1.939×10^{-3}	6.669×10^{-4}
$\nu_{c,\text{ref}} = \pi \log_e e^4 n_e \alpha / (\sqrt{2}^3 T_e^2)$	5.905×10^{-4}	2.229×10^{-3}
$\lambda_D^2 = \lambda_D^2 / \rho_s^2$	5.460×10^{-4}	6.962×10^{-4}
$\gamma_{E \times B} = -\frac{\alpha}{c_s} \frac{\rho}{q} \frac{d\Omega_{\text{tor}}}{d\rho}$	0.092	0.078
$\rho^* = \rho_s / \alpha$	1/353.2	1/532.7
$n_{\text{ref}} (= n_e) / 10^{19} \text{m}^{-3}$	2.107	1.653
$T_{\text{ref}} (= T_e) / \text{eV}$	992.2	436.1
$B_{\text{ref}} / \text{T}$	2.084	2.084
$L_{\text{ref}} (= \alpha) / \text{m}$	0.770	0.770
ρ_s / mm	2.183	1.447
$c_s / (\text{km/s})$	218.0	144.6
$\partial \rho / \partial (r/a)$	0.931	1.053

location is $r/a = 0.8$ which translates to $\rho = 0.739$ (instead of $\rho = 0.75$ as stated elsewhere).

B. Stability analysis with respect to the main physics parameters

As the transport underprediction could well be related to just slightly missing a threshold or critical value for mode excitation due to uncertainties in the input parameters, various (linear) parameter scans are demonstrated in the following. Variations of the gradients within the experimental error bars—estimated by 30%—are shown in Fig. 2. Clearly, no steep mode transition can be seen and while the dominant mode changes sign at lower toroidal wave numbers with increasing electron temperature gradient, it is only α/L_{T_i} which clearly affects the ITG growth rate as expected. An influence of the density gradient can hardly be seen. Further parameters which may alter the dominant mode are the

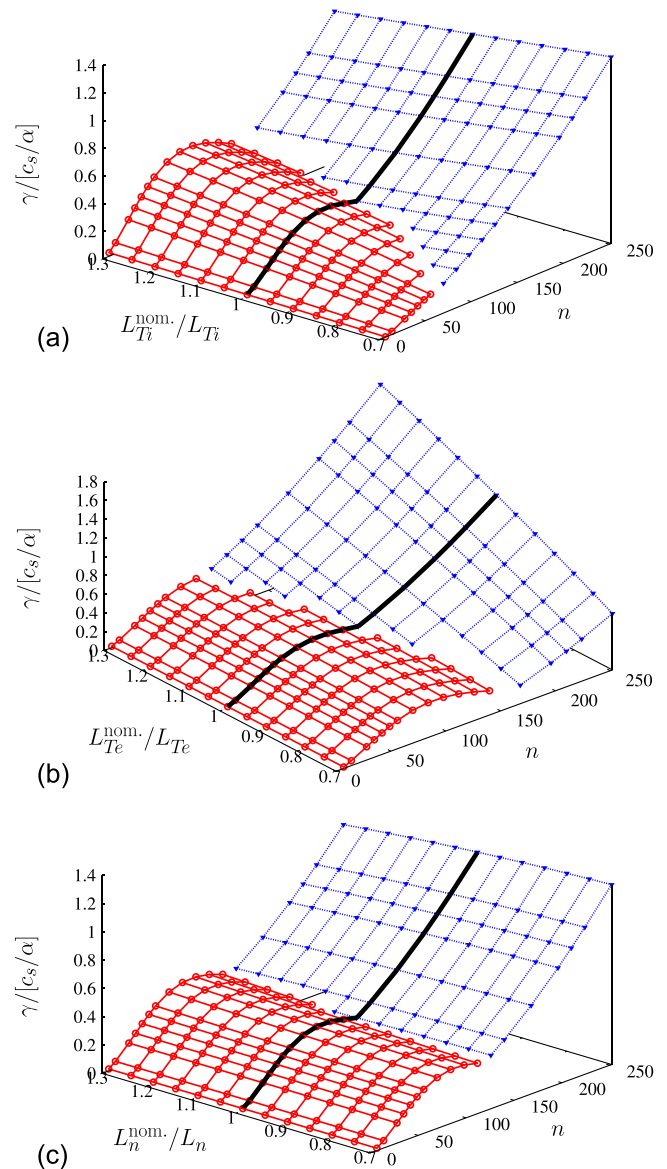


FIG. 2. Linear growth rate at $\rho = 0.739$ vs. low- k toroidal mode numbers n and temperature and density gradient variations within 30%. The spectra at the nominal values are indicated by black lines.

temperature ratio T_i/T_e , the collisionality, and the thermal-to-magnetic pressure ratio β . Their influence can be seen in Fig. 3. Variations of the temperature ratio are mainly changing the boundary in wave number space between the dominant modes drifting in ion- and electron-diamagnetic drift direction as can be expected for ITG and ETG modes which align to the ion and electron thermal velocity and gyroradii which directly depend on the temperature ratio. Here, however, the influence is rather marginal given that the presented 30% variation is clearly exaggerating—the experimental error bar is more likely on the order of 10%, see Ref. 10, Fig. 1. The collisionality and β do not have a significant impact when varied within the 30% range. However, the collisions *per se*

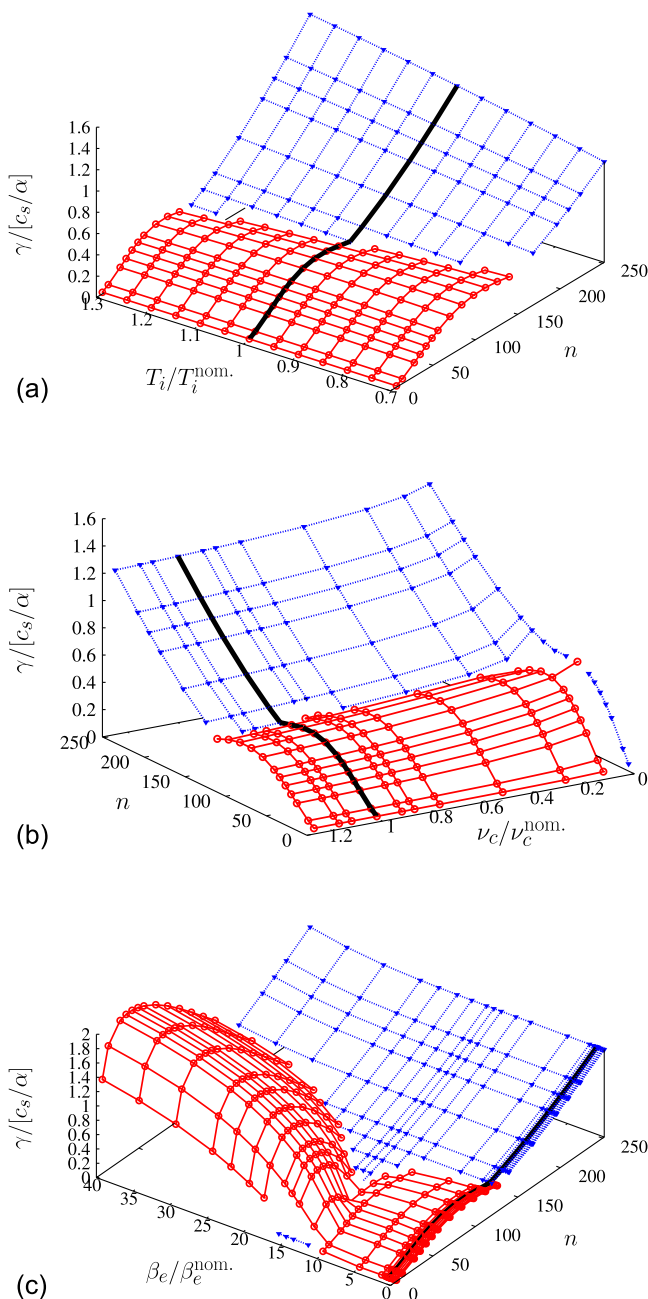


FIG. 3. Linear growth rate at $\rho = 0.739$ vs. low- k toroidal mode numbers n and (a) the temperature ratio T_i/T_e , (b) the collisionality, and (c) the plasma β (only in the field equations; the magnetic equilibrium is kept constant). The nominal values are indicated by black lines.

have strong impact on the dominant mode. Already at very small amplitude, they strongly reduce the TEMs being dominant in the collisionless case. The effect on the ITG mode taking over at finite collisionality is, however, almost negligible. Similarly, the β value. Only if increased by a factor of larger than 5 some stabilizing effect on the ITG modes can be found before Kinetic Ballooning Modes (KBM) take over at roughly 10 times the nominal value.

Summarizing, the most pronounced effect on the ion heat transport can be expected to originate from the ion temperature gradient for the radial position under consideration. Flux matching in nonlinear simulations should thus first be based on the adjustment of α/L_{Ti} and the $E \times B$ shearing rate which may very well be another possible regulator for ITG mode based ion heat transport. However, it should be noted that the nonlinear behavior may deviate from the linear, dominant mode based expectation, e.g., particularly in the vicinity of mode transitions and in the presence of substantial subdominant modes as is discussed, for instance, in Ref. 36. In the case at hand, TEMs are present as subdominant mode for nominal parameters, thus motivating further nonlinear studies.

IV. HEAT TRANSPORT IN FULLY NONLINEAR GYROKINETIC SIMULATIONS

This section is dedicated to the actual heat transport predictions based on nonlinear simulations. Before addressing the *shortfall* issue itself, contact is first made to previous studies at half-radius where previous benchmarking efforts have successfully taken place and where comparatively good agreement has been found between experiment and numerical simulation. Establishing similar findings with GENE is hence a natural step to be taken.

A. Inner-core validation and benchmark

A first test bed is defined in Ref. 21 where physical parameters for three species—deuterium, carbon impurities and electrons—are taken from the DIII-D discharge #128913 at $\rho = 0.5$ and used to run $E \times B$ -flow-free simulations in a Miller-type equilibrium.³⁷ Collisions are modeled by pitch-angle scattering and the number of toroidal modes has been fixed in the participating codes GYRO, GEM, and GS2. The nonlinear simulation results are summarized in Table II.

TABLE II. Electrostatic electron, ion, impurity, and combined (perpendicular) magnetic flutter heat transport fluxes $Q_{e,i,C}^{es}$, $Q_{B\perp}$ (here) normalized to $Q_{gb} = n_e T_e c_s \rho_s^2 / a^2$ together with the electron and ion particle fluxes $\Gamma_{e,i}$ in $\Gamma_{gb} = c_s \rho_s^2 / a$ gained from nonlinear (local) simulations at $\rho_{tor} = 0.5$. The GS2, GYRO, and GEM results are taken from Ref. 21, Table I. All simulations are run in Miller geometry, with pitch-angle collision operator and without $E \times B$ shear.

	GS2	GENE	GEM	GYRO
Q_e^{es}/Q_{gb}	5.24 ± 0.60	4.61 ± 0.31	4.00 ± 0.96	4.41 ± 0.54
Q_i^{es}/Q_{gb}	5.18 ± 0.64	4.51 ± 0.33	4.54 ± 1.06	4.03 ± 0.52
Q_C^{es}/Q_{gb}	0.14 ± 0.02	0.14 ± 0.01	0.10 ± 0.02	0.12 ± 0.01
$Q_{B\perp}/Q_{gb}$	0.05 ± 0.04	-0.02 ± 0.01	-0.06 ± 0.04	-0.10 ± 0.02
Γ_e/Γ_{gb}	0.84 ± 0.10	0.62 ± 0.05	0.62 ± 0.17	0.53 ± 0.08
Γ_i/Γ_{gb}	0.77 ± 0.10	0.52 ± 0.05	0.59 ± 0.17	0.47 ± 0.08

Here, GENE has been run with a radial box size of $L_x = 144.655\rho_s$ (here, $x = r$ is the average minor radius of the flux surface, $\rho_s = 2.183$ mm; a code-independent measure is $n_{xc} = 8$, the multiplier of the distance Δx between neighboring mode rational surfaces associated to the lowest finite n mode, $\Delta x = r/(qn_0\delta)$) and 192 radial grid points (wave numbers, respectively). The minimum toroidal wave number is $n_0 = 8$ ($k_y\rho_s = 0.0434$) and 16 toroidal wave numbers are considered in total.

Indeed, agreement within the error bars can be demonstrated for almost all observables defined in Ref. 21, i.e., for the electrostatic electron (Q_e), ion (Q_i), and impurity species (Q_C) heat transport fluxes, the combined electromagnetic heat transport ($Q_{B\perp}$) linked to perpendicular magnetic field fluctuations in gyroBohm units (here: $Q_{gB} = n_e T_e c_s \rho_s^2 / a^2$) as well as for the electron and ion particle fluxes. Hence, further confidence in the results of all four codes is provided—at least, in the given scenario neglecting $E \times B$ shear flows and assuming similar collision and geometry models. Corresponding investigations relaxing these constraints are on-going or future work.

The second point of contact is the GYRO results including $E \times B$ shear flow effects but restricting the simulation to kinetic deuterium and electron species. In Ref. 10, these are found to be slightly above the experimental value and almost on top of the experimental level if the shear flow strength is increased by 20%. Running GENE at this radial location yields similar results though a 10% change in the ion temperature gradient rather than an increase in the shear flow is considered. However, taking a closer look at the corresponding data points in Fig. 4 reveals that the nominal GENE value is somewhat larger which is on the one hand consistent with the 3 species benchmark result where GYRO reported the lowest values of all four codes. On the other hand, it might simply reflect that the simulations in Ref. 10 were performed approximately at $\rho = 0.5$. Comparing, e.g., the safety factor q in Refs. 10 and 21, reveals that the true position would be more like $\rho = 0.511$. Given the strong dependence on the gradients as found by GENE, a small change in the radial position already yields slightly different input parameters and hence transport level differences on the order as found in Fig. 4 at $\rho \approx 0.5$ are not surprising.

B. Outer-core transport simulation results

Having established reasonable agreement with previously published data and experimental levels at $\rho = 0.5$, the more interesting radial domain, namely, the outer-core ($\rho \geq 0.75$) is addressed in the following. Similar to Refs. 10 and 11, the simulated ion heat transfer rate first develops a trend opposing the ONETWO results—i.e., it decreases while the interpretation of the experimental values increases—as can be seen in Fig. 4(a). However, the underprediction in GENE is much less pronounced compared to Ref. 10—rather a factor of 2 than a factor of 6.7—and at $\rho = 0.85$ the predicted transport is furthermore again above the experimentally determined one. Amongst other uncertainties, this could be related to over- or underestimated ion temperature gradients as has been discussed in Sec. III. Corresponding scans can

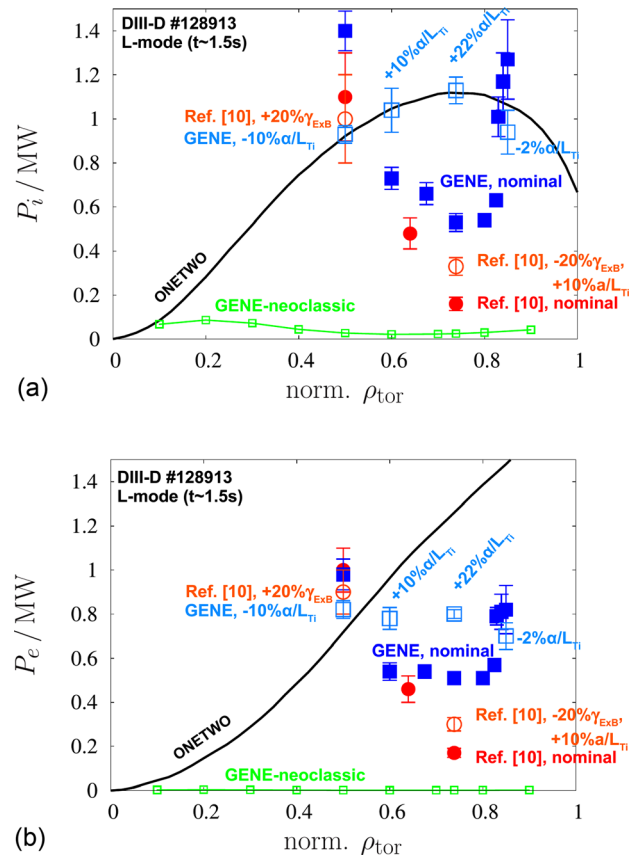


FIG. 4. Ion (a) and electron (b) heat transfer rates. The black line represents the ONETWO, the orange circles the gyrokinetic results taken from Ref. 10. The blue squares indicate the corresponding GENE results. Filled squares/circles represent the simulation results for nominal parameters, open circles/squares the best result when varying the input parameters within the range set by the accuracy of the measurement. For comparison, the neoclassical GENE result is added as well as green line and confirms the dominance of the anomalous transport in this discharge.

be found in Fig. 5, where a strong α/L_{Ti} dependence is indeed confirmed at various radial positions. Assuming the ion temperature gradient is the only uncertain parameter, the largest increase required for flux matching is 22% at $\rho = 0.7386$. However, even this value would be within the error bars as even small uncertainties in the temperature profile itself may translate to relatively large ones (up to $\sim 20\%$ – 30%) in the

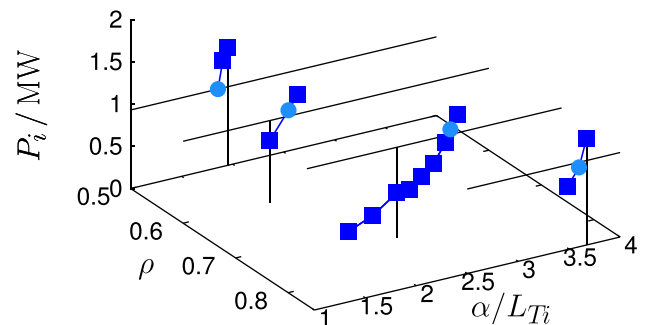


FIG. 5. Ion heat transfer rates vs. radius and ion temperature gradient, demonstrating the flux matching procedure. Dark blue squares indicate the individual GENE results and light blue circles the best match. Horizontal black lines represent the ONETWO value at that radius and vertical lines the nominal ion temperature gradient.

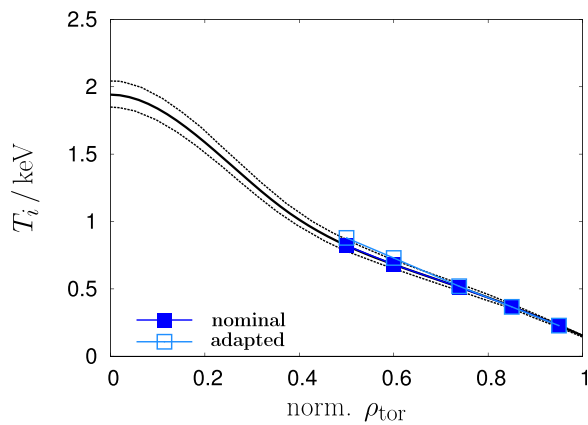


FIG. 6. Nominal ion temperature profile and profile reconstructed from flux matching gradients with the profile being fixed at $\rho = 0.9$. The reconstructed profile is still within the experimental error bars (dotted lines) found in Ref. 10.

gradients. A consistency check can be performed by reconstructing a new ion temperature profile by using the flux matched gradient values as it is done in Fig. 6. The result is within the error bars of the original profile and the modifications small enough that any effect of the modified T_e/T_i ratio can be neglected.

The whole approach here mimics an application of a transport solver being coupled to a gyrokinetic turbulence code as can be found in Refs. 38 and 39. Subject of the latter reference is even the discharge at hand. However, the profile is already fixed at $r/a = 0.7$ such that the radial range under question is excluded. Given the grid resolution being used by GENE, another such automated flux-matching attempt is not feasible at the moment due to the associated substantial computational costs.

Besides the ion temperature gradient, another important parameter possibly affecting the turbulence under consideration is the $\mathbf{E} \times \mathbf{B}$ shear flow and the parallel flow shear which is consistently evolved in GENE. Hence, a corresponding sensitivity scan at $\rho = 0.7386$ can be found in Fig. 7. Clearly

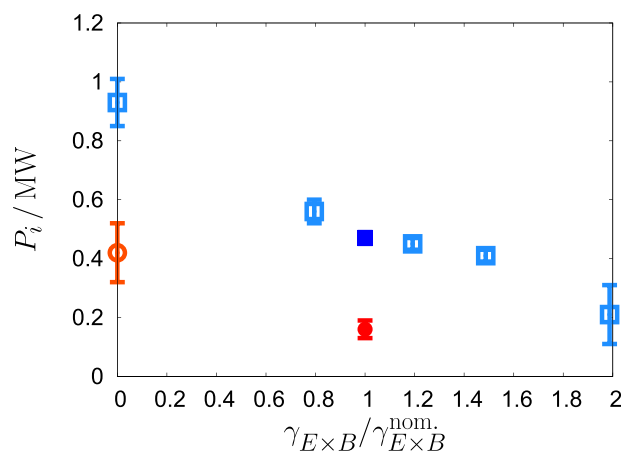


FIG. 7. Time-averaged ion heat transfer rates at $\rho = 0.7386$ as function of the (external) $\mathbf{E} \times \mathbf{B}$ shear flow amplitude. For comparison, the results extracted from Ref. 10 are displayed as well. Here, the unsheared value has been estimated from a time trace and hence been labeled with a large error bar.

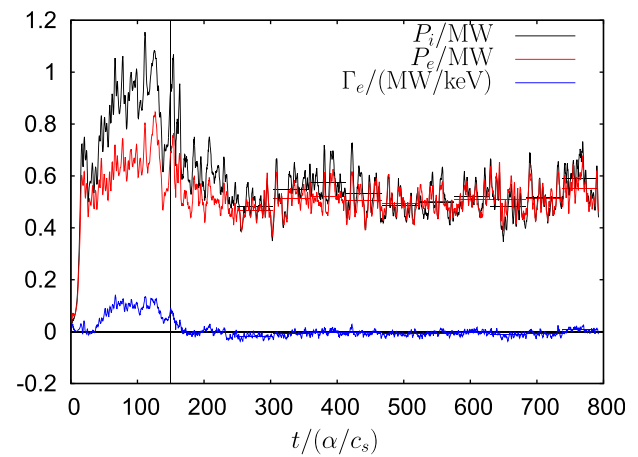


FIG. 8. Time traces of flux-surface averaged heat and particle transfer rates at $\rho = 0.7386$ using default parameters. The vertical line indicates the point in time at which the external $\mathbf{E} \times \mathbf{B}$ shear flow is activated. Time averages are taken starting at $t = 250\alpha/c_s$, the individual subwindows for the statistical error span 5 correlation times ($t_{\text{corr}} = 10.7\alpha/c_s$) and are included as vertical lines.

here and in Fig. 8, the turbulence level drops significantly about a factor of two as soon as the additional shearing is activated as can be anticipated given the associated eddy tilting and breaking. However, within 20% variations about the nominal shear flow amplitude reflecting the maximum error bars in Ref. 10, the ion heat transfer rate is only modestly changed ($\sim 20\%$) compared to its response to similar ion temperature gradient variations where about a factor of two has been observed. Compared to the transport levels from Ref. 10, the shearing effect seems to be somewhat weaker—the reduction is rather a factor of 2 than approximately 2.6. The differing shear flow implementations in both codes may thus explain some fraction of the observed discrepancy. However, even in the unsheared case, the ion heat transfer rate presented here exceeds the one in Ref. 10 by a factor of about 2 (about 3 including the shearing).

Before discussing details regarding numerical convergence, the simulation data presentation shall be completed with the spectra of the transfer rates. Qualitatively, they do agree well with those found in Ref. 10, Fig. 4(b). For instance, a particle pinch is found at smaller scales while an outward flow can be observed below toroidal mode numbers $n \lesssim 60$. The ion heat channel appears to be well resolved with only very small contributions at the lowest and largest finite wave numbers. The electron heat flux spectrum, on the contrary, does not decay towards zero at largest resolved wave numbers. This is in line with previous notions regarding possible small-scale ETG contributions and could hence explain the remaining P_e discrepancy in Fig. 4(b) even with increased α/L_{Ti} . Indeed, running a single-scale simulation restricted to electron gyroradius scales and with adiabatic ions gave additional 0.45 MW of electron heat transfer rate which would pretty much compensate the missing fraction. The P_e underprediction hence appears to be of less concern. However, a final answer could strictly speaking only be gained via multiscale simulations covering ion- and electron-gyroradius-scales self-consistently which is beyond this work.

Returning to the spectra, it is furthermore noteworthy that the heat flux peak positions are similar as well—the toroidal mode number at peak position is $n_{\text{peak}} = 60$ in Ref. 10 and $n_{\text{peak}} = 49$ in Fig. 9. The slight downshift is also reflected in a steeper decay to smaller wave numbers and might be linked to the differing shear flow models which preferably act on these spatial scales. However, summarizing, the spectra do not provide indications for entirely different physics—rather the opposite. Only the amplitudes appear to be scaled compared to Ref. 10.

C. Numerical convergence tests

With two different code predictions at hand, particular emphasis should be given to numerical convergence both in grid numbers and sizes in great detail. First of all, the perpendicular directions are addressed as the safety factor and the magnetic shear become quite large in the outer-core range, thus typically requiring larger boxes due to the former⁴⁰ and higher radial resolution to compensate for the latter. The corresponding results are summarized in Fig. 10 where radial and binormal spectra are shown for the default grids and for increased box size or resolution. Clearly, neither of these variations yields substantial deviations, which is furthermore reflected by the total ion heat transfer rates which do not vary much, i.e., within the range of the statistical error bars. Numerical convergence can thus be ensured in the first two dimensions. Addressing the remaining directions has been done by simultaneously increasing the resolution by at least a factor of 1.5. The result can be found in Table III and hardly differs from the reference.

Further simulation results to be found here are, e.g., comparisons with and without an effective ion charge $Z_{\text{eff}} = 1.334$ in the collision operator, an approach which is often used in two-species simulations to mimic at least parts of the effect of the missing impurities. The ion heat flux indeed responds with a 10% reduction which can be further enhanced to almost 14% by employing a collision operator based on pitch-angle scattering instead of the linearized Landau-Boltzmann operator. On the other hand, approximating the slightly up-down-asymmetric flux surface shape by a

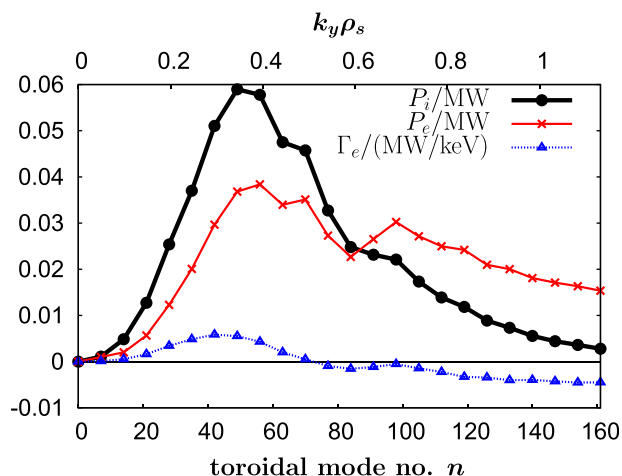


FIG. 9. Time-averaged heat and particle transfer rate spectra vs. binormal wave number $k_y \rho_s$ or toroidal mode number n , respectively, at $\rho = 0.7386$.

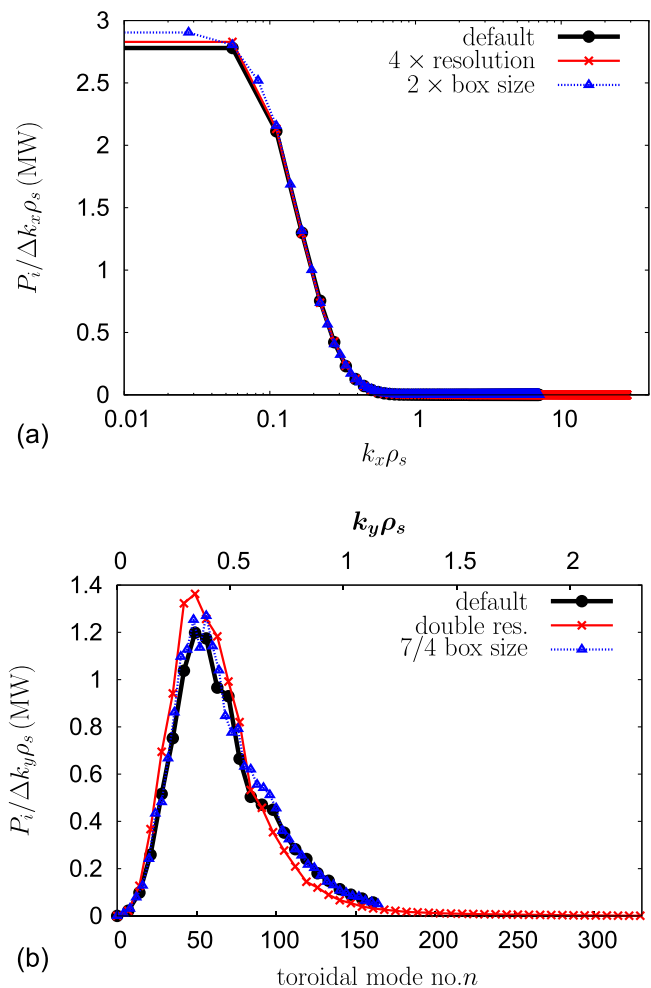


FIG. 10. Time-averaged radial (a) and binormal (b) spectra of the ion heat transfer rate P_i for different box sizes (minimum wave numbers) and resolutions (number of modes). The total ion heat transport seems to be reasonably well captured with the default choice of grid numbers and box sizes ($L_x = 114 \rho_s$ ($n_{\text{exc}} = 10$) and $n_0 = 7$).

Miller parametrization has hardly any effect—both of these models are used in Ref. 10. The simultaneous usage and furthermore the application of similar grids and physical input parameters as in the reference publication again yields results very similar to the default GENE case with

TABLE III. Nonlinear simulation results at $\rho = 0.7386$ for different resolutions or physical models. The differences compared to the default grid $n_x \times n_y \times n_z \times n_v \times n_w = 256 \times 24 \times 16 \times 32 \times 8$ or in the choice of the collision operator (default: linearized Landau-Boltzmann) or MHD equilibrium (default: efit tracing) are indicated in the first column.

Variation	P_i (MW)	P_e (MW)	Γ_e (MW/keV)
$Z_{\text{eff}} = 1$: default	0.52 ± 0.04	0.51 ± 0.02	-0.01 ± 0.01
$Z_{\text{eff}} = 1.334$: default	0.47 ± 0.02	0.49 ± 0.01	-0.01 ± 0.0
(n_z, n_v, n_w) = (48, 48, 16)	0.47 ± 0.02	0.48 ± 0.01	-0.01 ± 0.0
pitch-angle collisions	0.45 ± 0.05	0.51 ± 0.04	-0.05 ± 0.01
Miller equilibrium	0.51 ± 0.03	0.48 ± 0.02	-0.01 ± 0.0
Miller equilibrium, pitch-angle collision, Ref. 10 parameters	0.52 ± 0.05	0.53 ± 0.04	-0.04 ± 0.01
(n_x, n_y) = (320, 16)			

$Z_{\text{eff}} = 1.334$ —except for the particle flux which generally appears to be larger with pitch-angle scattering.

The almost unchanged ion heat transfer rate can be explained by a cancellation of the pitch-angle scattering related reduction with slightly larger gradients between those listed in Ref. 10 and those independently extracted from the data base.

V. VALIDATION BEYOND TRANSPORT COMPARISONS

The set of diagnostics available at DIII-D allows for a much more detailed comparison and validation of the turbulence simulations beyond the transport comparisons employed above. For instance, temperature and density fluctuation amplitudes as well as the cross phases between these fluctuating quantities can be addressed and assessed regarding their impact on the transport levels.

However, accurately comparing the fluctuation amplitudes requires the implementation and application of sophisticated synthetic diagnostics as described in Ref. 10. The setup being used here to model Beam Emission Spectroscopy (BES) and Correlation Electron Cyclotron Emission (CECE) is very similar and can be summarized as follows. First, temporally high-resolved 3D density and temperature fluctuations are translated from co-moving to laboratory-frame by adding a corresponding phase factor to the Fourier space data. After the transform to configuration space, the data is mapped and interpolated from fluxtube to torus geometry by exploiting the toroidal periodicity and the quasi-periodic boundary condition in the direction parallel to the magnetic field which are inherent to fluxtube simulations. For now, BES and CECE are considered as 2D filters and hence only particular poloidal cuts are convoluted with appropriate 2D point spread functions (PSFs) modelling the (R, Z) extend of the individual BES and CECE channels. The resulting data are processed in the same way as in the experiment, for instance, by computing cross-power spectra with the same subroutine. It should be noted that—unlike Ref. 10 which used numerical PSFs taken from Ref. 41 for the BES—asymmetric Gaussians are employed which approximate the numerical shapes with Gaussian widths taken from Ref. 41. By comparison with symmetric Gaussians, an impact of the shape on the signal can be confirmed. It does, however, not affect the qualitative results and has rather small effect on the quantitative findings. The synthetic BES density fluctuations—or, more precisely, the cross-power frequency spectra—for the nominal gradient and the flux-matched GENE simulation at $\rho = 0.7384$ can be found in Fig. 11, together with the experimental measurements and the reference simulation results from Ref. 10. First of all, even the GENE signal based on the nominal parameters is significantly larger than in previous gyrokinetic simulation attempts which is consistent with the heat fluxes, see Fig. 4. Like in Ref. 10, the spectral shape is already close to the experimentally measured one. However, the amplitudes are underestimated. The root-mean-square (RMS) averaged density fluctuation in the 40–400 kHz window is 0.50% compared to 1.1% in the experiment and 0.33% in Ref. 10. As can be seen in Fig. 11, the agreement is significantly improved with the increased ion temperature gradient where the RMS value is 0.71%. The remaining discrepancy could

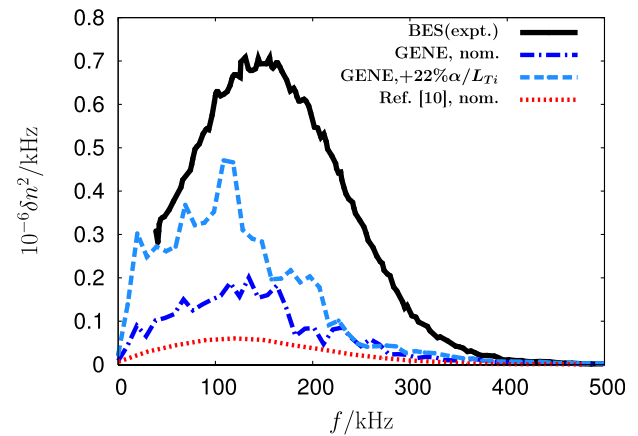


FIG. 11. Cross-power frequency spectra of electron density fluctuations for the shortfall discharge at $\rho \approx 0.74$. Besides BES data from experiment, synthetic BES results from gyrokinetic GENE simulations with nominal and increased ion temperature gradient and corresponding simulations from Ref. 10 are shown.

point towards the necessity of running additional sensitivity scans, e.g., in the density gradient in order to match this observable more accurately or could indicate the need for further refinement of the synthetic diagnostic. For instance, any temperature fluctuation impact on the beam emission intensity is currently neglected in line with Ref. 10. However, as the current degree already appears to be reasonable, this task is left for future work—together with another refinement suggested in Ref. 42. Here, 2D spectra of the correlation between the BES channels have been compared between BES measurements and synthetic GYRO results and demonstrated a modest but notable disparity that might reflect a difference in how finite ExB shear impacts turbulence.

The CECE diagnostics at DIII-D allows for similar comparisons for the electron temperature fluctuations. Cross-power spectra from synthetic CECE diagnostics with nominal gradient and flux-matched GENE simulation data are plotted together with those from Ref. 10 and the experimental measurements in Fig. 12. Consistent with the heat flux

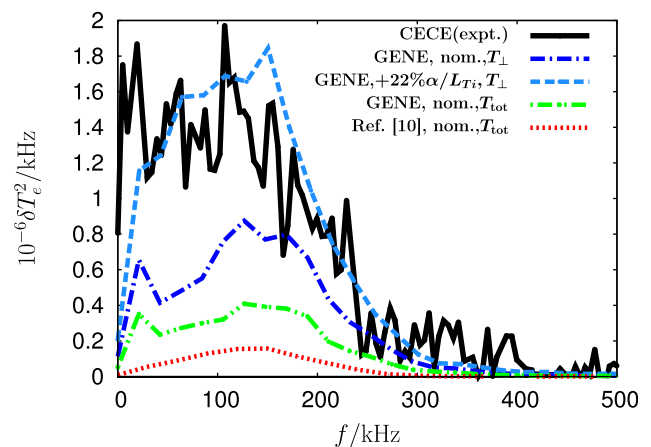


FIG. 12. Cross-power frequency spectra of electron temperature fluctuations for the shortfall discharge at $\rho \approx 0.74$. Synthetic CECE results taken from gyrokinetic GENE simulations with nominal and increased ion temperature gradient are compared to the corresponding results in Ref. 10 and to the actual experimental data. Furthermore, the difference in using perpendicular or total electron temperature fluctuations for synthetic CECE is depicted.

observations, the synthetic electron temperature fluctuations from GENE are again much larger than those from Ref. 10 when using the nominal parameters.

However, maybe even more strikingly, significantly more low frequency contributions can be found with GENE, whereas the simulation in Ref. 10 fails to reproduce this trend. The latter may be decisive for explaining the shortfall as low frequency components are found to be dominant in the experiment. Furthermore, it should be noted that *total* temperature fluctuations have been used in the aforementioned reference and hence for the direct code-code comparison at hand. However, the CECE diagnostics should be more or even exclusively susceptible for the *perpendicular* temperature component. With GENE's native velocity space coordinates v_{\parallel} and μ , the separation into parallel and perpendicular components is straight-forward and the synthetic CECE results with T_{\perp} only are shown in Fig. 12 as well. The agreement with the experimentally measured signal is indeed significantly improved for the nominal

parameters and very impressive in the case of the flux-matched simulation where the spectral shapes almost match. This is also reflected in the RMS temperature fluctuations in the aforementioned frequency window. With total temperature fluctuations and nominal parameters, 0.82% are found compared to 0.50% in Ref. 10. Due to the strong anisotropy of the fluctuations, this value increases to 1.20% when considering the perpendicular component only. Finally, considering the flux-matched simulation, the (perpendicular) electron temperature fluctuation level is 1.72% which is well within the error bars of the measured signal $1.6\% \pm 0.2\%$.

Another observable of interest are cross phases as they—together with the fluctuation amplitudes—determine the transport level. Here, they are defined as $\alpha(A \times B) = \tan^{-1}(\text{Im}(A/B)/\text{Re}(A/B))$ for two observables A and B . If the latter—for instance, radial electric field and density fluctuations—are shifted by $\pi/2$, i.e., electrostatic potential and density fluctuations are in phase, no particle transport $\Gamma^{\text{es}} \sim \langle n_1 v_{E \times B} \rangle$ can be established as is approximately

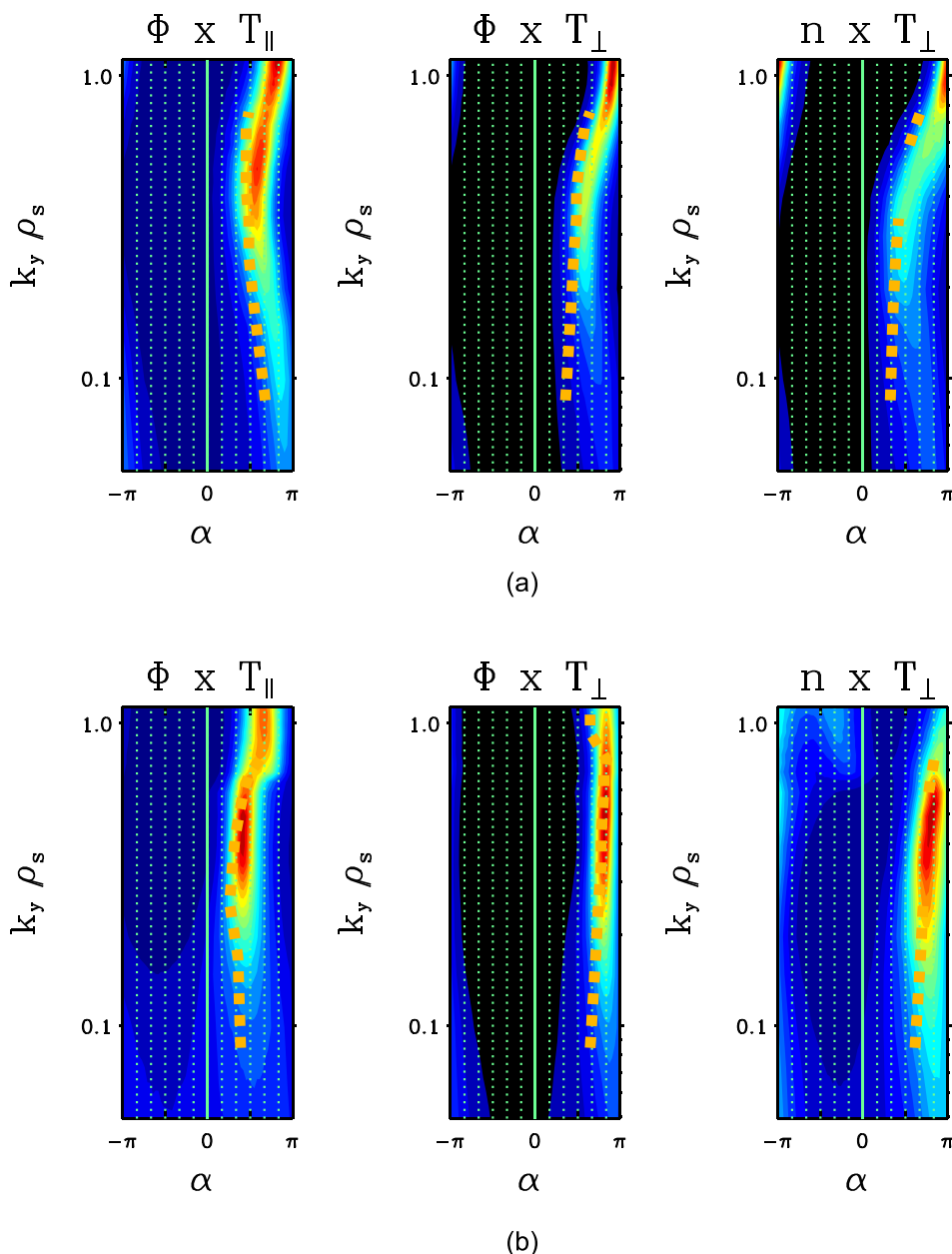


FIG. 13. Time-averaged cross-phases $\alpha(A \times B)$ between indicated observables for (a) ions and (b) electrons as function of the binormal wave number at $\rho = 0.7386$. The histogram is based on the values at all radial and parallel grid points and weighed by amplitude. For comparison, the corresponding linear results are added as dashed, orange line.

achieved in the present scenario. Hence, Fig. 13 displays the remaining linear and nonlinear cross phases relevant for the electrostatic heat transport—the electromagnetic fraction is negligible anyway. Clearly, the phase relation between the electrostatic potential and both ion temperature components is most favorable, i.e., near to $\pi/2$, around $k_y \rho_s = 0.15 - 0.8$ and tending towards a phase shift of π at largest wave numbers thus substantially reducing the transport. For the electron counterparts, however, the phase shift is less pronounced moving from $\pi/2$ to π which explains the residual electron heat flux at these scales. A third column displays the density and perpendicular temperature cross phases as functions of the binormal wave number. Comparing with the second column it becomes apparent that ϕ_1 and n_1 are indeed approximately in phase.

However, more importantly these results can be compared with experimental measurements hence extending the options for validation. Though not available for the discharge discussed above (#128913), experimental results can be found for a very similar discharge in Ref. 43, Fig. 8. At $\rho = 0.75$, the experimentally observed phase shift between the electron density and perpendicular electron temperature fluctuations is $101^\circ \pm 8^\circ$ with reversed sign due to contrary

definitions used here. The corresponding GENE simulation result using the #128913 profile input in the approximate wave number range of the diagnostics $0.2 \lesssim k_y \rho_s \lesssim 0.4$ is on the same order but higher at about 135° . However, running another set of dedicated GENE simulations with the input parameters taken from the profiles of this sibling discharge (#138040) yields a significantly improved agreement. As can be seen in Fig. 14, the cross-phase is now about 103° in the aforementioned wave number range. Furthermore, good experiment-simulation agreement is also demonstrated at another radial location ($\rho = 0.65$) and for an additional scenario with electron cyclotron heating as additional power input (discharge #138038). We note in passing that none of the simulations for the additional discharges has found a substantial shortfall. Concluding this paragraph, confidence for GENE matching the correct cross phase reasonably well in the shortfall case can be considered to be high.

In summary, the GENE simulations for the original DIII-D shortfall appear to be very realistic. Cross-phase predictions for similar discharges where the corresponding experimental diagnostics had been available seem to be very robust and in good agreement. With appropriate synthetic diagnostics modeling and slight adaptations of the temperature profile within the error bars, whole BES and CECE cross-power spectra can be validated to a very high degree. In this context, the necessity to implement synthetic CECE diagnostics with the perpendicular temperature fluctuation component only has been demonstrated.

VI. CONCLUSIONS

After a number of successful and encouraging validation studies with local δf gyrokinetic simulations, e.g., in L-mode inner-core and H- and QH-mode regimes, a series of publications reported failures in similar attempts for outer-core L-mode plasmas—known as “shortfall.” While significant underpredictions of the electron heat transport could very well be related to unresolved scales, no such explanation is available for the ion counterpart. Hence, various concerns regarding the applicability of fluxtube simulations, the validity of common approximations in the implementations, or even the gyrokinetic theory itself have been raised for this general type of plasmas. However, with more recent local gyrokinetic studies addressing outer-core L-modes in other devices and matching the ion heat flux within experimental error bars of the input parameters,^{12,14} the original conclusion seems to be less universal. Furthermore, no effort had been undertaken so far to investigate the original scenarios independently with another implementation and interface to the experiment.

This deficit has been overcome in the present contribution where the plasma microturbulence code GENE has been applied to one of the L-mode discharges where a gyrokinetic shortfall had been observed for the first time. In agreement with previous findings, the ion heat transport is indeed found to be underpredicted around $\rho \sim 0.75$ while the simulation results tend to be even larger than in the experiment in the deep core regime at $\rho = 0.5$. However, the shortfall is much less pronounced and can be removed by mild changes of the ion temperature profile within the experimental error bars.

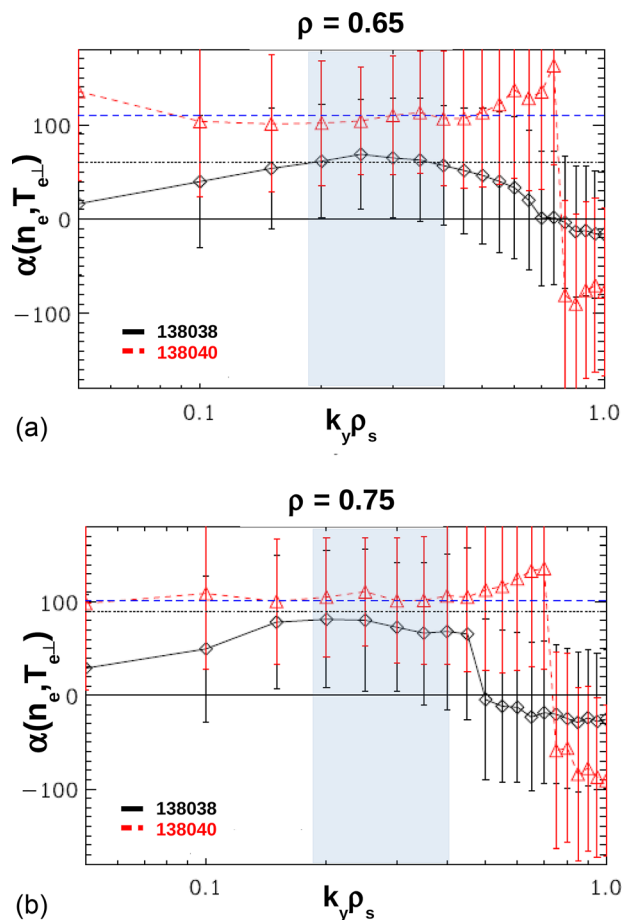


FIG. 14. Time-averaged mean $(n_e, T_{\perp,e})$ cross-phases from nonlinear, local simulations for DIII-D discharges #138038 and #138040 at two radial positions ($\rho_{\text{tor}} = 0.65, 0.75$) as function of the binormal wave number. The error bars represent the standard deviation from the cross-phase distribution (as shown in Fig. 13). The experimental values⁴³ are included as dashed blue (#138040) and dotted black (#138038) lines. The relevant range for comparison due to diagnostics constraints is indicated by the shaded region.

Furthermore, even the nominal transport levels tend to overestimate rather than underestimate the experimental results around $\rho \sim 0.85$ again. Finally, extended validation studies involving cross-phases and synthetic BES and CECE signals have demonstrated a high degree of realism and hence provide further confidence in the presented GENE simulations.

The validity of the GENE results has furthermore been substantiated by benchmarks with other codes at inner core positions and the demonstration of numerical convergence. All in all, the total computational effort invested in the above tasks is quite substantial. About 5 MCPUH had to be employed for physical and numerical parameter scans.

In summary, even local δf gyrokinetic simulations seem to be sufficiently adequate to capture the main features of the L-mode discharge and the radial position under consideration. This does not exclude further improvements by the additional consideration of nonlocal effects, particularly at even larger radii. However, concerns regarding a possible breakdown of gyrokinetic theory appear to be premature in this parameter regime. A comparison with the previous study of this discharge¹⁰ reveals that both codes are describing quite similar physics—transport spectra, for instance, demonstrate remarkable qualitative agreement in all three channels shown. However, the quantitative disagreement is an open question and subject to on-going collaborative verification efforts.

ACKNOWLEDGMENTS

The authors gratefully acknowledge valuable discussions with G. W. Hammett, H. Doerk, G. R. McKee, M. J. Pueschel, and R. Bravenec. The simulations presented in this work were carried out using the HELIOS supercomputer system at Computational Simulation Centre of International Fusion Energy Research Centre (IFERC-CSC), Aomori, Japan, and the SUPERMUC supercomputer at Leibniz-Rechenzentrum (LRZ), Garching, Germany. This work has been carried out within the framework of the EUROfusion Consortium and has received funding from the European Union's Horizon 2020 research and innovation programme under Grant Agreement No. 633053. The views and opinions expressed herein do not necessarily reflect those of the European Commission.

¹A. J. Brizard and T. S. Hahm, *Rev. Mod. Phys.* **79**, 421 (2007).

²X. Garbet, Y. Idomura, L. Villard, and T. H. Watanabe, *Nucl. Fusion* **50**, 043002 (2010).

³J. A. Krommes, *Annu. Rev. Fluid Mech.* **44**, 175 (2012).

⁴J. Candy and R. Waltz, *Phys. Rev. Lett.* **91**, 045001 (2003).

⁵A. Casati, T. Gerbaud, P. Hennequin, C. Bourdelle, J. Candy, F. Clairet, X. Garbet, V. Grandgirard, Ö. D. Gürcan, S. Heuraux, G. T. Hoang, C. Honoré, F. Imbeaux, R. Sabot, Y. Sarazin, L. Vermare, and R. E. Waltz, *Phys. Rev. Lett.* **102**, 165005 (2009).

⁶C. Holland, L. Schmitz, T. L. Rhodes, W. A. Peebles, J. C. Hillesheim, G. Wang, L. Zeng, E. J. Doyle, S. P. Smith, R. Prater, K. H. Burrell, J. Candy, R. E. Waltz, J. E. Kinsey, G. M. Staebler, J. C. Deboo, C. C. Petty, G. R. McKee, Z. Yan, and A. E. White, *Phys. Plasmas* **18**, 056113 (2011).

⁷C. Holland, C. C. Petty, L. Schmitz, K. H. Burrell, G. R. McKee, T. L. Rhodes, and J. Candy, *Nucl. Fusion* **52**, 114007 (2012).

⁸J. Candy and R. E. Waltz, *J. Comput. Phys.* **186**, 545 (2003).

⁹J. L. Luxon, *Nucl. Fusion* **42**, 614 (2002).

¹⁰C. Holland, A. E. White, G. R. McKee, M. W. Shafer, J. Candy, R. E. Waltz, L. Schmitz, and G. R. Tynan, *Phys. Plasmas* **16**, 052301 (2009).

¹¹T. L. Rhodes, C. Holland, S. P. Smith, A. E. White, K. H. Burrell, J. Candy, J. C. Deboo, E. J. Doyle, J. C. Hillesheim, J. E. Kinsey, G. R. McKee, D. Mikkelsen, W. A. Peebles, C. C. Petty, R. Prater, S. Parker, Y. Chen, L. Schmitz, G. M. Staebler, R. E. Waltz, G. Wang, Z. Yan, and L. Zeng, *Nucl. Fusion* **51**, 063022 (2011).

¹²N. T. Howard, A. E. White, M. Greenwald, M. L. Reinke, J. Walk, C. Holland, J. Candy, and T. Görler, *Phys. Plasmas* **20**, 032510 (2013).

¹³Y. Ren, W. Guttenfelder, S. M. Kaye, E. Mazzucato, R. E. Bell, A. Diallo, C. W. Domier, B. P. LeBlanc, K. C. Lee, M. Podesta, D. R. Smith, and H. Yuh, *Nucl. Fusion* **53**, 083007 (2013).

¹⁴D. Told, F. Jenko, T. Görler, F. J. Casson, E. Fable, and ASDEX Upgrade Team, *Phys. Plasmas* **20**, 122312 (2013).

¹⁵R. E. Waltz and Z. Deng, *Phys. Plasmas* **20**, 012507 (2013).

¹⁶A. M. Dimits, G. Bateman, M. A. Beer, B. I. Cohen, W. Dorland, G. W. Hammett, C. Kim, J. E. Kinsey, M. Kotschenreuther, A. H. Kritiz, L. L. Lao, J. Mandrekas, W. M. Nevins, S. E. Parker, A. J. Redd, D. E. Shumaker, R. Sydora, and J. Weiland, *Phys. Plasmas* **7**, 969 (2000).

¹⁷W. M. Nevins, J. Candy, S. Cowley, T. Dannert, A. Dimits, W. Dorland, C. Estrada-Mila, G. W. Hammett, F. Jenko, M. J. Pueschel, and D. E. Shumaker, *Phys. Plasmas* **13**, 122306 (2006).

¹⁸M. J. Pueschel, M. Kammerer, and F. Jenko, *Phys. Plasmas* **15**, 102310 (2008).

¹⁹A. E. White, L. Schmitz, W. A. Peebles, T. A. Carter, T. L. Rhodes, E. J. Doyle, P. A. Gourdain, J. C. Hillesheim, G. Wang, C. Holland, G. R. Tynan, M. E. Austin, G. R. McKee, M. W. Shafer, K. H. Burrell, J. Candy, J. C. Deboo, R. Prater, G. M. Staebler, R. E. Waltz, and M. A. Makowski, *Rev. Sci. Instrum.* **79**, 103505 (2008).

²⁰A. E. White, L. Schmitz, G. R. McKee, C. Holland, W. A. Peebles, T. A. Carter, M. W. Shafer, M. E. Austin, K. H. Burrell, J. Candy, J. C. Deboo, E. J. Doyle, M. A. Makowski, R. Prater, T. L. Rhodes, G. M. Staebler, G. R. Tynan, R. E. Waltz, and G. Wang, *Phys. Plasmas* **15**, 056116 (2008).

²¹R. V. Bravenec, Y. Chen, J. Candy, W. Wan, and S. Parker, *Phys. Plasmas* **20**, 104506 (2013).

²²F. Jenko, W. Dorland, M. Kotschenreuther, and B. N. Rogers, *Phys. Plasmas* **7**, 1904 (2000).

²³T. Görler, X. Lapillonne, S. Brunner, T. Dannert, F. Jenko, F. Merz, and D. Told, *J. Comput. Phys.* **230**, 7053 (2011).

²⁴J. Candy, R. E. Waltz, and W. Dorland, *Phys. Plasmas* **11**, L25 (2004).

²⁵B. F. McMillan, X. Lapillonne, S. Brunner, L. Villard, S. Jolliet, A. Bottino, T. Görler, and F. Jenko, *Phys. Rev. Lett.* **105**, 155001 (2010).

²⁶F. Merz, "Gyrokinetic simulation of multimode plasma turbulence," Ph.D. thesis (Westfälische Wilhelms-Universität Münster, 2008).

²⁷P. Xanthopoulos and F. Jenko, *Phys. Plasmas* **13**, 092301 (2006).

²⁸G. W. Hammett, W. Dorland, N. F. Loureiro, and T. Tatsuno, in *APS Meeting Abstracts* (American Physical Society, Philadelphia, 2006) p. 1136.

²⁹H. Doerk, F. Jenko, M. J. Pueschel, and D. R. Hatch, *Phys. Rev. Lett.* **106**, 155003 (2011).

³⁰W. Guttenfelder, J. Candy, S. M. Kaye, W. M. Nevins, E. Wang, R. E. Bell, G. W. Hammett, B. P. Leblanc, D. R. Mikkelsen, and H. Yuh, *Phys. Rev. Lett.* **106**, 155004 (2011).

³¹H. Doerk, F. Jenko, T. Görler, D. Told, M. J. Pueschel, and D. R. Hatch, *Phys. Plasmas* **19**, 055907 (2012).

³²F. Jenko, *J. Plasma Fusion Res. SERIES* **6**, 11 (2004).

³³T. Görler and F. Jenko, *Phys. Rev. Lett.* **100**, 185002 (2008).

³⁴T. Görler and F. Jenko, *Phys. Plasmas* **15**, 102508 (2008).

³⁵N. T. Howard, A. E. White, M. L. Reinke, M. Greenwald, C. Holland, J. Candy, and J. R. Walk, *Nucl. Fusion* **53**, 123011 (2013).

³⁶F. Merz and F. Jenko, *Nucl. Fusion* **50**, 054005 (2010).

³⁷R. L. Miller, M. S. Chu, J. M. Greene, Y. R. Lin-Liu, and R. E. Waltz, *Phys. Plasmas* **5**, 973 (1998).

³⁸M. Barnes, I. G. Abel, W. Dorland, T. Görler, G. W. Hammett, and F. Jenko, *Phys. Plasmas* **17**, 056109 (2010).

³⁹J. Candy, C. Holland, R. E. Waltz, M. R. Fahey, and E. Belli, *Phys. Plasmas* **16**, 060704 (2009).

⁴⁰M. Barnes, F. I. Parra, and A. A. Schekochihin, *Phys. Rev. Lett.* **107**, 115003 (2011).

⁴¹M. W. Shafer, R. J. Fonck, G. R. McKee, and D. J. Schlossberg, *Rev. Sci. Instrum.* **77**, 10F110 (2006).

⁴²M. W. Shafer, R. J. Fonck, G. R. McKee, C. Holland, A. E. White, and D. J. Schlossberg, *Phys. Plasmas* **19**, 032504 (2012).

⁴³A. E. White, W. A. Peebles, T. L. Rhodes, C. H. Holland, G. Wang, L. Schmitz, T. A. Carter, J. C. Hillesheim, E. J. Doyle, L. Zeng, G. R. McKee, G. M. Staebler, R. E. Waltz, J. C. Deboo, C. C. Petty, and K. H. Burrell, *Phys. Plasmas* **17**, 056103 (2010).